SHOCK-WAVE STRUCTURE ON HYBRID POWER-LAW LEADING EDGES IN HYPERSONIC FLOW

Wilson F. N. Santos

wilson@lcp.inpe.br

Combustion and Propulsion Laboratory

National Institute for Space Research

Cachoeira Paulista, SP, 12630-000, BRAZIL

Abstract. *The aim of the work reported here is to describe the computational investigation of a rarefied hypersonic flow past hybrid power-law shaped leading edges. The work is motivated by interest in assessing the overall performance of hybrid power-law leading edges in order to consider them as possible candidates for blunting geometries of hypersonic configurations. The shape impact on the shock-wave structure has been investigated by employing the Direct Simulation Monte Carlo (DSMC) method. A method that has become the main technique for studying complex multidimensional rarefied flows, and that properly accounts for the non-equilibrium aspects of the flows. The results presented highlight the sensitivity of shock-wave standoff distance, shock-wave thickness and shock-wave shape to changes on the upper-surface shape of the leading edges. The analysis showed that the asymmetry on the leading-edge shape causes the expected asymmetry on the shock-wave patterns. It was also found that the shock standoff and the shock thickness decreased by increasing the upper-surface power-law exponent.*

Keywords: Hypersonic flow, Rarefied flow, DSMC, shock standoff, hybrid power-law shape.

1. INTRODUCTION

Hypersonic waverider configurations have been proposed as promising airframes for high-speed vehicles because they have the highest known lift-drag (*L/D*) performance. Waveriders are aerodynamic configurations whose design is based on known supersonic or hypersonic flowfield. Generated by an inverse method from streamlines behind a known shock wave, the waverider lower surface is a stream surface of a known inviscid flow around a reference body, for instance, behind planar oblique shock wave (Nonweiler, 1959), behind conical shock waves around circular or elliptical cones (Rasmussen, 1980, and Kim, Rasmussen and Jischke, 1983), behind power-law shocks (Rasmussen and Duncan, 1995, Mazhul and Rakchimov, 2004, and Mangin et al., 2006), as well as the flows in converging cone ducts (Goonko, Nazhul and Markelov, 2000).

Waverider-based hypersonic vehicle must operate in a wide range of freestream Mach number. When flying at its design Mach number, the entire bow shock is attached to the leading edge of the body. The attached shock wave may prevent spillage of high-pressure airflow from the lower side of the vehicle to the upper side, resulting in a high-pressure differential and enhanced lift. It is the shock attachment that produces de high *L/D* ratio observed in waverider vehicles.

Nevertheless, at hypersonic flight speeds, the vehicle leading edges should be blunt to some extent in order to reduce the heat transfer rate to acceptable levels and to allow for internal heat conduction. The use of blunt-nose shapes tends to alleviate the aerodynamic heating problem since the heat flux for blunt bodies is far lower than that for sharply pointed bodies. Therefore, due mainly to manufacturing problems and the extremely high temperatures attained in hypersonic flight, hypersonic vehicles should have blunt nose, although probably slendering out at a short distance from the nose. Nonetheless, geometric bluntness results in shock-wave detachment. Thus, the loss of shock-wave attachment will allow pressure leakage from the lower side of the vehicle to the upper side, thereby degrading the aerodynamic performance of waverider vehicles.

In this scenario, power-law shaped leading edges ($y \propto x^p$, $0 < p < 1$) may provide the required bluntness for heat transfer and manufacturing concerns with less increase in shock-wave detachment so that the final design more closely approximates the ideal aerodynamic performance. This concept is based on work of Mason and Lee (1994) that pointed out, based on Newtonian flow analysis, that these shapes exhibit both blunt and sharp aerodynamic properties. They suggested the possibility of a difference between shapes that are geometrically sharp and shapes that behave aerodynamically as if they were sharp. According to them, for values in the range of $0 < p < 1$, the slope of the power-law shape is infinite at $x = 0$, a characteristic of a blunt body. However, for $1/2 < p < 1$, the radius of curvature at the nose approaches zero, a characteristic of a sharp body.

A great deal of experimental and theoretical works has been carried out previously on power-law form representing blunt geometries. Of particular interest are the works by Santos and Lewis (2002, 2005a, and 2005b) and by Santos (2005, and 2008a). The major interest in these works has gone into considering the power-law shape as possible candidate for blunting geometries of hypersonic waverider leading edge.

Santos and Lewis (2002 and 2005b) have investigated power-law shapes in rarefied hypersonic flow through the use of the Direct Simulation Monte Carlo (DSMC) method. They found that the stagnation point heating behavior for power-law leading edges with finite radius of curvature, $p = 1/2$, followed that predicted for classical blunt body in that the heating rate is inversely proportional to the square root of curvature radius at the stagnation point. For those power-law leading edges with zero radii of curvature, $p > 1/2$, it was found that the stagnation point heating is not a function of the curvature radius at the vicinity of the leading

edges, but agreed with the classical blunt body behavior predicted by the continuum flow far from the stagnation point. Results were compared to a corresponding circular cylinder to determine which geometry would be better suited as a blunting profile. Their analysis also showed that power-law shapes provided smaller total drag than circular cylinder, typically used in blunting sharp leading edges for heat transfer considerations. However, circular cylinder provided smaller stagnation point heating than power-law shapes under the range of conditions investigated.

In order to assess the advantages and disadvantages of a power-law body, computational results are obtained for a different scenario of power-law shapes. In the present account, the shock-wave structure is investigated for hybrid power-law shapes, i.e., lower and upper surfaces with different power-law exponents. In this connection, the purpose of this work is to examine computationally the leading-edge shape effects on the shock-wave standoff distance, shock-wave thickness and shock-wave shape of hybrid or asymmetric power-law leading edges in order to provide information on how well these shapes stand up as possible candidates for blunting geometries of hypersonic leading edges. The impact on the shock-wave structure due to changes on the leading-edge shape will be investigated for a combination of power-law exponents of 1/2, 3/5, 2/3 and 3/4 for the upper and lower surface shapes.

2. LEADING-EDGE GEOMETRY

In dimensional form, the body power-law shapes are given by the following expression,

$$y = Ax^p \tag{1}$$

where p is the power-law exponent and A is the power-law constant, which is a function of p.

In the previous work (Santos and Lewis, 2002), the symmetric power-law shapes were modeled by assuming a sharp-edged wedge of half angle θ with a circular cylinder of radius R inscribed tangent to this wedge. The symmetric power-law shapes, inscribed between the wedge and the cylinder, are also tangent to them at the same common point where they have the same slope angle. The circular cylinder diameter provides a reference for the amount of blunting desired on the leading edges. It was assumed a leading-edge half angle of 10 degrees, a circular cylinder diameter of 10^{-2}m and power-law exponents of 1/2, 3/5, 2/3, 7/10, 3/4, and 4/5. Figure 1(a) illustrates schematically this construction for the set of symmetric power-law leading edges previously investigated.
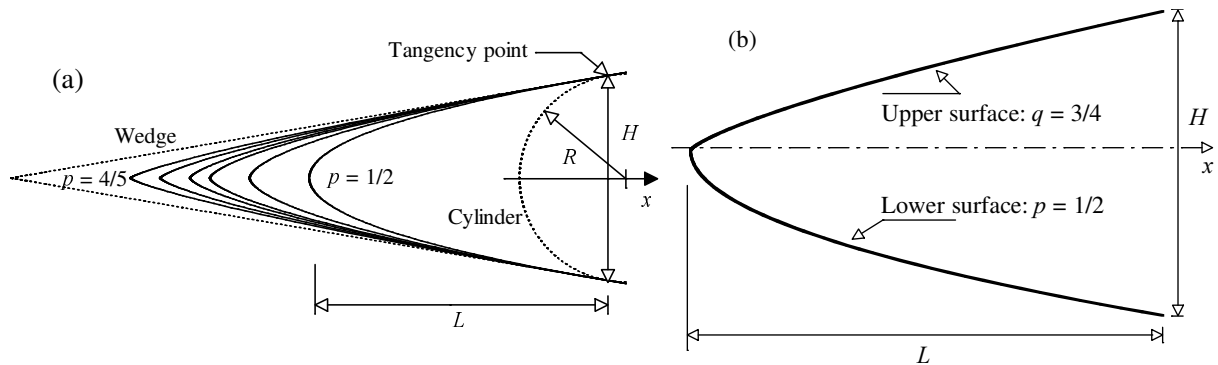

Figure 1: Drawing illustrating the (a) symmetric and (b) the asymmetric power-law leading edges.

From geometric considerations, the common body height H, Fig. 1(a), at the tangency point is equal to $2Rcos\theta$. The power-law constant A, obtained by matching slope on the wedge, circular cylinder and power-law body at the tangency point is given as follows,

$$A = \frac{\left(\dfrac{R^2}{1+\tan^2\theta}\right)^{(1-p)/2}}{\left(\dfrac{p}{\tan\theta}\right)^p}$$

(2)

As the slope of the power-law shapes is infinite at $x = 0$, i.e., the slope angle is 90 degrees, the asymmetric or hybrid power-law shapes were obtained by combining the upper and lower part of the curves, with respect to the symmetry line, shown in Fig. 1(a). In this way, for the hybrid power-law shapes, the upper surface was represented by the exponent q of 1/2, 3/5, 2/3 or 3/4 and the lower surface by the exponent p of 1/2. Figure 1(b) illustrates an asymmetric or hybrid power-law leading edge defined by $q = 3/4$ and $p = 1/2$. It was assumed that the hybrid power-law leading edges are infinitely long but only the length L is considered in the simulation since the wake region behind the power-law bodies is not of interest in this investigation.

3. COMPUTATIONAL TOOL

The option of the numerical approach in order to model rarefied non-equilibrium flows relies on the extent of flow rarefaction. For near-continuum flows, the boundary conditions of slip velocity and temperature jump are enough to take into account for the rarefaction effects. These boundary conditions are commonly employed in the Navier-Stokes equations or in the viscous shock layer equations. The Navier-Stokes equations can be derived from the Boltzmann equation (Cercignani, 1988) under the assumption of small deviation of the distribution function from equilibrium. Nevertheless, the Navier-Stokes equations become unsuitable for studying rarefied flows where the distribution function becomes considerable non-equilibrium.

In order to study flows with a significant degree of non-equilibrium, the DSMC method (Bird, 1994), pioneered by Bird in the 60's, has become the standard technique employed. The DSMC method simulates real gas flows with various physical processes by means of a huge number of modeling particles, each of which is a typical representative of great number of real gas molecules. DSMC models the flow as being a collection of discrete particles, each one with a position, velocity and internal energy. The state of particles is stored and modified with time as the particles move, collide, and undergo boundary interactions in simulated physical space. The simulation is always calculated as unsteady flow. However, a steady flow solution is obtained as the large time state of the simulation. Therefore, the DSMC method is basically an explicit time-marching algorithm.

Collisions in the present DSMC code are modeled by using the variable hard sphere (VHS) molecular model (Bird, 1981) and the no time counter (NTC) collision sampling technique (Bird, 1989). Repartition energy among internal and translational modes is controlled by the Borgnakke-Larsen statistical model (Borgnakke and Larsen, 1975). Simulations are performed using a non-reacting gas model for a constant freestream gas composition consisting of 76.3% of N_2 and 23.7% of O_2. Energy exchanges between the translational and internal modes, rotational and vibrational, are considered. Relaxation collision numbers of 5 and 50 were used for the calculations of rotation and vibration, respectively.

4. COMPUTATIONAL FLOW DOMAIN AND GRID

In order to implement the particle-particle collisions, the flowfield is divided into an arbitrary number of regions, which are subdivided into computational cells. The cells are further subdivided into four subcells, two subcells/cell in each direction. The cell provides a convenient reference sampling of the macroscopic gas properties, whereas the collision partners are selected from the same subcell for the establishment of the collision rate. As a result, the flow resolution is much higher than the cell resolution. The dimensions of the cells must be such that the change in flow properties across each cell is small. The linear dimensions of the cells should be small in comparison with the distance over which there is a significant change in the flow properties. These conditions define that the cell dimensions should be of the order of the local mean free path or even smaller (Alexander et al., 1998 and 2000).

The computational domain used for the calculation is made large enough so that body disturbances do not reach the upstream and side boundaries, where freestream conditions are specified. A schematic view of the computational domain is depicted in Fig. 2. Side I is defined by the body surface. Diffuse reflection with complete thermal accommodation is the condition applied to this side. Side II is the freestream side through which simulated molecules enter and exit. Finally, side III is the downstream outflow boundary. At this boundary, the flow is predominantly supersonic and vacuum condition is specified (Guo and Liaw, 2001). As a result, it is assumed that at this boundary simulated molecules can only exit.
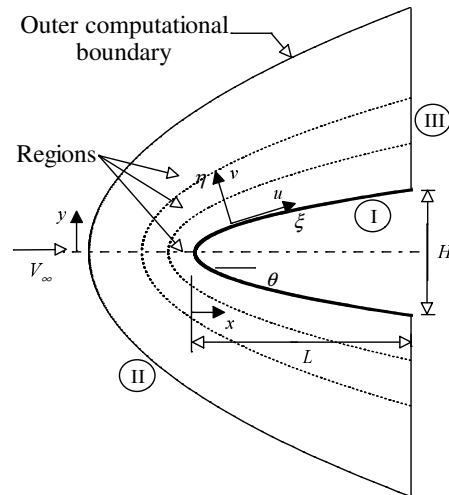
Figure 2: Drawing illustrating the computational domain.

The effects of grid resolution and the effects of the number of particles per computational cell were investigated in order to determine the number of cells and the number of particles required to achieve grid independence solutions. In this fashion, a grid independence study was made with three different structured meshes in each coordinate direction. The effect of altering the cell size in the ξ-direction was investigated with grids of 60(coarse), 90(standard) and 120(fine) cells on the upper and lower surfaces, and 60 cells in the η-direction for the leading edges investigated. In analogous manner, an examination was made in the η-direction with grids of 30(coarse), 60(standard) and 90(fine) cells, and 90 cells along the upper and lower surface, i.e., in the ξ-direction. In addition, each grid was made up of non-uniform cell spacing in both directions. The effect (not shown) of changing the cell size in both directions

on the heat transfer and pressure coefficients was rather insensitive to the range of cell spacing considered, indicating that the standard grid, 180x60 cells in the entire domain is essentially grid independent. A similar procedure was performed with respect to the number of particles. The total number of particles depends on the case investigated. On the average, it is around of 350,000 particles.

5. COMPUTATIONAL CONDITIONS

DSMC simulations have been performed for an altitude of 70 km based on the flow conditions given by Santos and Lewis (2002) and summarized in Table 1, and the gas properties (Bird, 1994) are shown in Table 2. Referring to Tables 1 and 2, T_∞, p_∞, ρ_∞, n_∞, μ_∞ and λ_∞ stand respectively for temperature, pressure, density, number density, viscosity and mean free path, and X, m, d and ω account respectively for mole fraction, molecular mass, molecular diameter and viscosity index.

The freestream velocity V_∞ is assumed to be constant at 3.56 km/s. This velocity corresponds to a freestream Mach number M_∞ of 12. The translational and vibrational temperatures in the freestream are in equilibrium at 220 K. The wall temperature T_w is assumed constant at 880 K. This temperature is chosen to be representative of the surface temperature near the stagnation point and is assumed to be uniform over the entire surface of the leading edges.

The freestream Knudsen number Kn_∞, defined as the ratio of the molecular mean free path λ in the freestream gas to a characteristic dimension of the flowfield, corresponds to 0.0903, where the characteristic dimension was defined as being the diameter of the reference circular cylinder (see Fig. 1). The freestream Reynolds number Re_∞ by unit meter is 21,455.

Table 1: Freestream Conditions

Altitude (km)	T_∞ (K)	p_∞ (N/m^2)	ρ_∞ x 10^5 (kg/m^3)	n_∞ x 10^{-21} (m^{-3})	μ_∞ x 10^5 (Ns/m^2)	λ_∞ x 10^3 (m)	V_∞ (m/s)
70	220.0	5.582	8.753	1.8209	1.455	0.903	3560

Table 2: Gas Properties

	X	m (kg)	d (m)	ω
O$_2$	0.237	5.312 x 10^{-26}	4.01 x 10^{-10}	0.77
N$_2$	0.763	4.65 x 10^{-26}	4.11 x 10^{-10}	0.74

6. COMPUTATIONAL PROCEDURE

The problem of predicting the shape and location of detached shock waves has been stimulated by the necessity for blunt noses and leading edges configurations designed for hypersonic flight in order to cope with the aerodynamic heating. In addition, the ability to predict the shape and location of shock waves is of primary importance in analysis of aerodynamic interference. Furthermore, the knowledge of the shock-wave displacement is especially important in waveriders (Nonweiler, 1959), since these hypersonic configurations usually rely on shock-wave attachment at the leading edges to achieve their high lift-to-drag ratio at high-lift coefficient.

In the present account, the shock-wave structure, defined by shape, thickness and detachment of the shock wave, is predicted by employing a procedure based on the physics of the particles (Santos, 2008a). In this respect, the flow is assumed to consist of three distinct classes of molecules; class I molecules denote those molecules from freestream that have not been affected by the presence of the leading edge; class II molecules designate those molecules that, at some time in their past history, have struck and been reflected from the body surface; and finally, class III molecules define those molecules that have been indirectly affected by the presence of the body. Figure 3(a) illustrates the definition for the molecular classes.

In this manner, it is assumed that the class I molecule changes to class III molecule when it collides with class II or class III molecule. Class I or class III molecule is progressively transformed into class II molecule when it interacts with the body surface. Also, a class II molecule remains class II regardless of subsequent collisions and interactions. Hence, the transition from class I molecules to class III molecules may represent the shock wave, and the transition from class III to class II may define the boundary layer.

A typical distribution of class III molecules along the stagnation streamline for blunt leading edges is displayed in Fig. 3(b) along with the definition used to determine the thickness, displacement and shape of the shock wave. In this figure, X is the distance x along the stagnation streamline (see Fig. 2), normalized by the freestream mean free path λ_∞, and f_{III} is the number of molecules for class III to the total amount of molecules inside each cell.
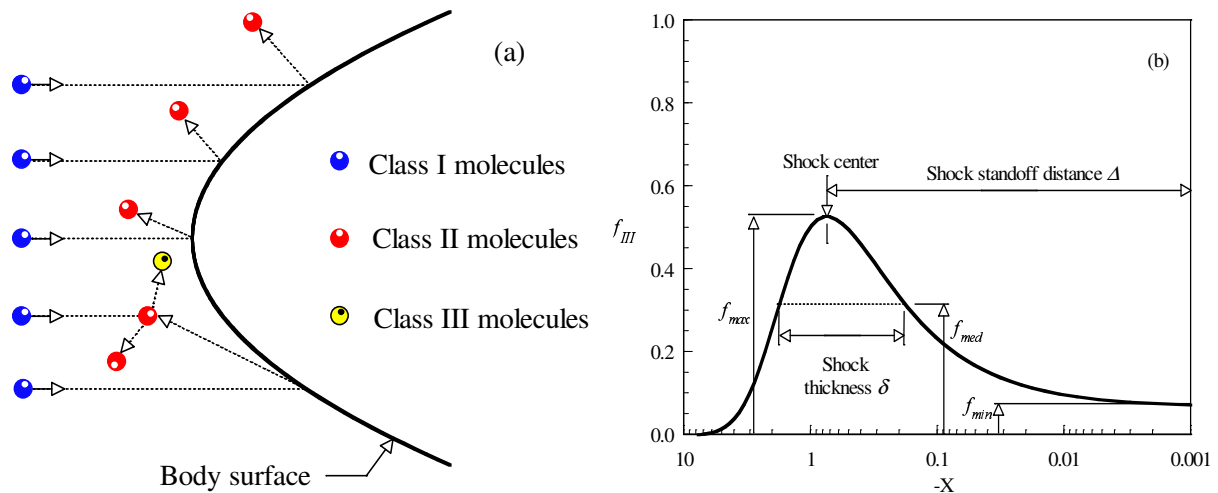

Figure 3: (a) Drawing illustrating the classification of molecules and (b) Schematic of shock-wave structure.

In a rarefied flow, the shock wave has a finite region that depends on the transport properties of the gas, and it can no longer be considered as a discontinuity obeying the classical Rankine-Hugoniot relations. In this context, the shock-wave standoff distance Δ is defined as being the distance between the shock wave center and the nose of the leading edge along the stagnation streamline. As shown in Fig. 3(b), the center of the shock wave is defined by the station that corresponds to the maximum value for f_{III}. The shock-wave thickness δ is defined by the distance between the stations that correspond to the mean value for f_{III}. Finally, the shock-wave shape (shock wave "location") is determined by the coordinate points given by the maximum value in the f_{III} distribution along the lines departing from the body surface, i.e., η-direction as shown in Fig. 2.

7.   COMPUTATIONAL RESULTS AND DISCUSSION

The purpose of this section is to discuss and to compare differences in the displacement, thickness and shape of the shock wave due to variations on the leading-edge shape. Before proceeding with the analysis of the shock-wave structure, it is desirable to highlight the major features of the results related to the molecular class distribution.

7.1   Molecular Class Distribution

The distribution of molecules for classes I, II and III along the stagnation streamline is displayed in Figs. 4, 5 and 6 for power-law exponent q of 3/5, 2/3, and 3/4, respectively. In this set of plots, f_I, f_{II} and f_{III} are the ratios of the number of molecules for class I, II and III, respectively, to the total amount of molecules inside each cell along the stagnation line. X represents the upstream length x along the stagnation line normalized by λ_∞. In addition, p and q refer to the power-law exponents of the lower- and upper-surface shapes, respectively. For comparison purpose, the distribution of molecules for classes I, II and III for the symmetric leading edges ($q = p$) is also displayed in this group of figures. In this way, empty and filled symbols in this set of plots correspond to the symmetric and asymmetric leading edges, respectively. Finally, the flow direction is from left to right as defined by Fig. 2.

Looking first at Figs. 4(a) and 4(b), it is clearly seen that changes on the leading-edge shape affects the shock-wave structure, as would be expected. As the upper-surface power-law exponent q changes from 1/2 to 3/5, the presence of the leading edge is felt slightly less upstream. This behavior is observed by the location of the maximum value for f_{III} in Fig. 4(a). This is explained by the fact that the leading edge defined by $q = 3/5$ is sharper than that defined by $q = 1/2$. Conversely, as the lower-surface power-law exponent p changes from 3/5 to 1/2, Fig. 4(b), the leading edge becomes slightly blunter and the presence of the leading edge is felt more upstream with respect to the stagnation point. As a result, changes on the shape of the leading edge will affect the displacement, thickness and shape of the shock wave in a different manner.

Turning next to Figs. 5 and 6, it may be recognized that the sharper the leading edge becomes, i.e., by increasing the power-law exponent q, the smaller the upstream disturbance along the stagnation line.
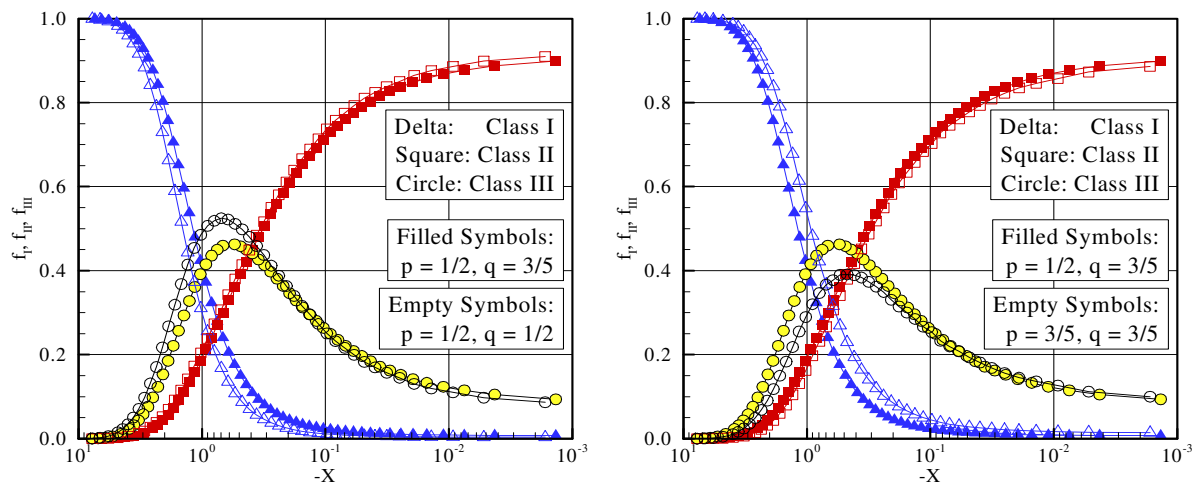

Figure 4: Distribution of molecules for classes I, II and III along the stagnation streamline for leading edge defined by power-law exponents of $p = 1/2$ and $q = 3/5$. (a) Comparison with symmetric leading edge defined by $p = q = 1/2$ and (b) $p = q = 3/5$.

Of great significance in Figs. 4, 5, and 6 is the behavior of the class I molecules for sharp and blunt leading edges. It should be observed that molecules from freestream, represented by class I molecules, basically do not reach the nose of the leading edges even after the establishment of the steady state. This is shown in Fig. 4(a), for the $p = q = 1/2$ case, which represent a blunt leading edge case. In contrast, molecules from freestream collide with the nose of the leading edge for that case illustrated in Fig. 6(b), $p = q = 3/4$ case, which represents a sharp leading edge. This is explained by the fact that density increases much more at the vicinity of the stagnation region for blunt leading edges (Santos and Lewis, 2002), and reaches its maximum value in the stagnation point. In this connection, the buildup of particle density near the nose of the leading edge acts as a shield for the molecules coming from the undisturbed stream. It is very encouraging to observe that the asymmetric power-law leading edges basically follow the same trend as those symmetric leading edges.
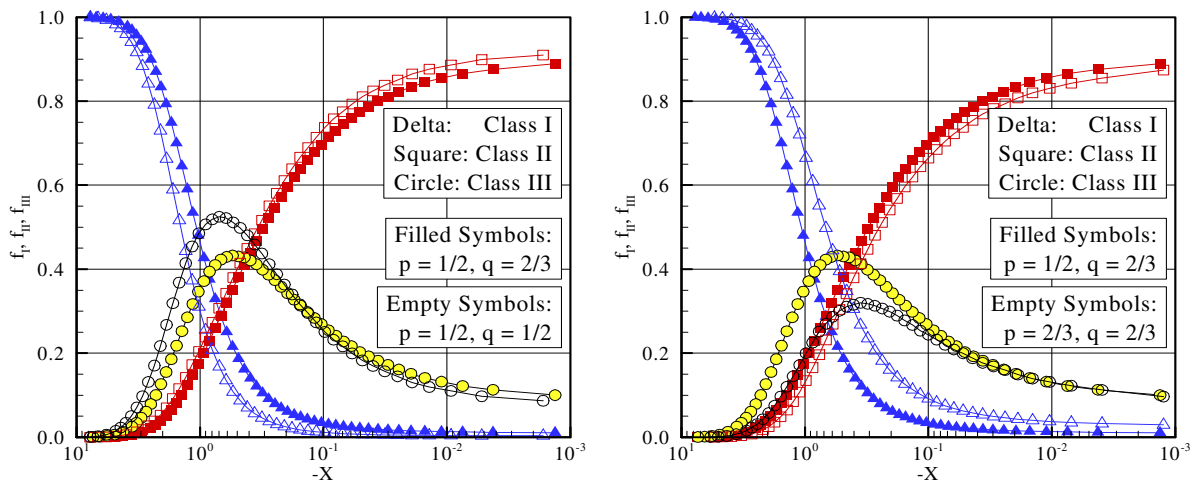

Figure 5: Distribution of molecules for classes I, II and III along the stagnation streamline for leading edge defined by power-law exponents of $p = 1/2$ and $q = 2/3$. (a) Comparison with symmetric leading edge defined by $p = q = 1/2$ and (b) $p = q = 2/3$.
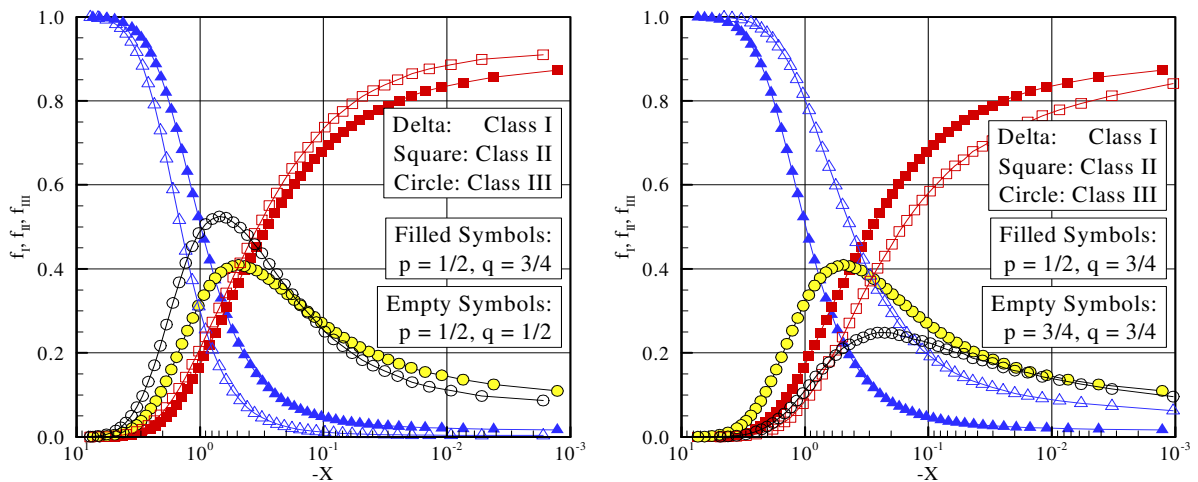

Figure 6: Distribution of molecules for classes I, II and III along the stagnation streamline for leading edge defined by power-law exponents of $p = 1/2$ and $q = 3/4$. (a) Comparison with symmetric leading edge defined by $p = q = 1/2$ and (b) $p = q = 3/4$.

7.2 Shock-Wave Standoff Distance

The shock-wave standoff distance Δ can be obtained from Figs. 4, 5 and 6 for the cases shown. Based on the shock displacement definition presented in Fig. 3(b), the calculated shock-wave standoff distance Δ, normalized by the freestream mean free path λ_∞, is tabulated in Table 3 for the cases investigated.

Table 3: Dimensionless shock-wave standoff distance Δ/λ_∞ along the stagnation line for symmetric and asymmetric power-law leading edges.

	$q = 1/2$	$q = 3/5$	$q = 2/3$	$q = 3/4$
$p = 1/2$	0.678	0.576	0.523	0.483
$p = 3/5$		0.459		
$p = 2/3$			0.343	
$p = 3/4$				0.231

It is apparent from the results on Table 3 that there is a discrete shock standoff distance for the cases investigated. As would be expected, the shock standoff distance increases with decreasing the power-law exponent for the symmetric leading-edge shape; since the leading edge becomes blunt with decreasing the power-law exponent p. It is also seen that, the shock standoff distance along the stagnation line decreased with increasing the power-law exponent of the upper surface as compared to the exponent of the lower surface. By increasing the upper-surface power-law exponent, the leading edge becomes a sharp leading edge.

It should be remarked that shock standoff distance becomes important in hypersonic vehicles such as waveriders, which depend on leading-edge shock attachment to achieve their high L/D ratio at high lift coefficient. In this connection, symmetric power-law leading edge seems to be more appropriate, since it presents reduced shock wave detachment distances as compared to that of asymmetric or hybrid power-law leading edge. Nevertheless, it should be mentioned in this context that a smaller shock detachment distance is associated with a higher heat load to the nose of the body.

As a base of comparison, the heat transfer coefficient C_{ho} at the stagnation point corresponds approximately to 0.605, 0.672, 0.703, and 0.739 (Santos, 2008b) for leading-edge shapes given by power-law exponent q of 1/2, 3/5, 2/3 and 3/4, respectively. Nonetheless, the heat transfer coefficient at the stagnation point for symmetric power-law leading edges (Santos and Lewis, 2002) with exponents ($p = q$) of 3/5, 2/3 and 3/4 is 0.730, 0.785 and 0.858, respectively. Consequently, it is firmly established that the hybrid power-law leading edges investigated present a smaller heat transfer coefficient at the stagnation point than their corresponding symmetric power-law leading edges.

7.3 Shock-Wave Thickness

According to the definition for shock-wave thickness illustrated in Fig. 2(b), the shock wave thickness δ along the stagnation streamline can be calculated from Figs. 3 and 4 for the leading edges cases displayed. As a result of the calculation, Table 4 tabulates the shock-wave thickness δ, normalized by the freestream mean free path λ_∞, for all cases investigated. In a similar way, the values presented are for the shock-wave thickness along the symmetry line and the stagnation line.

It is evident from Table 4 that, in general, the shock-wave thickness follows the same trend presented by the shock-wave standoff distance along the stagnation line in that it

decreases with increasing the power-law exponent of the upper surface as compared to the exponent of the lower surface.

Table 4: Dimensionless shock wave thickness δ/λ_∞ along the stagnation line for symmetric and asymmetric power-law leading edges.

	$q = 1/2$	$q = 3/5$	$q = 2/3$	$q = 3/4$
$p = 1/2$	1.586	1.352	1.247	1.147
$p = 3/5$		1.110		
$p = 2/3$			0.887	
$p = 3/4$				0.642

7.4 Shock-Wave Shape

The shock-wave shape, defined by the shock wave center location, is obtained by calculating the position that corresponds to the maximum f for class III molecules in the η-direction along the body surface (see Fig. 2(b)).

Comparison of the shock-wave shape on symmetric and asymmetric power-law leading edges is illustrated in Figs. 7, 8, and 9 for upper-surface power-law exponents of 3/5, 2/3 and 3/4, respectively. In an effort to emphasize points of interest, a magnified view of the shock-wave shapes at the vicinity of the leading-edge nose is shown in this group of figures. Also, in this set of plots, the dimensionless length X and height Y are the Cartesian coordinates x and y normalized by λ_∞.
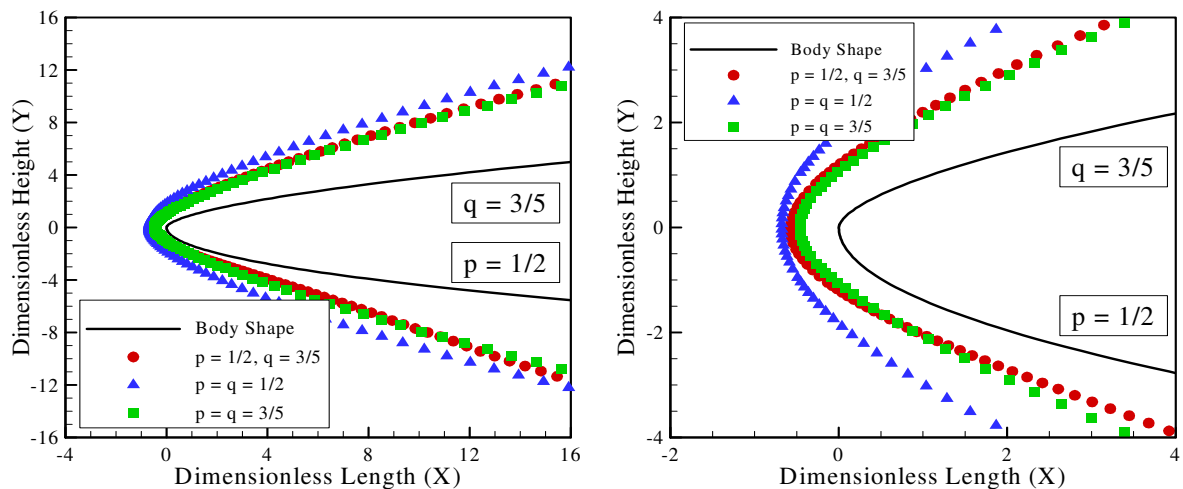
Figure 7: Shock-wave shapes on power-law leading edge defined by $p = 1/2$ and $q = 3/5$: (a) shock-wave on the total leading edge and (b) magnified view at the vicinity of the leading-edge nose.

It is seen from this set of plots that increasing the upper-surface power-law exponent causes the expected asymmetry in the shock wave patterns with respect to the leading-edge centerline. As a result of the geometric asymmetry, the net buildup of particle density decreases in the upper side and it increases in the lower side (Santos, 2008b) with increasing the power-law exponent q. Consequently, the presence of the leading edge, propagated by random motion of the molecules, is communicated to a larger distance away from the body on

the upper side than that on the lower side. Hence, the shock wave center locates more away of the body surface on the upper side and closer to the body surface on the lower side.
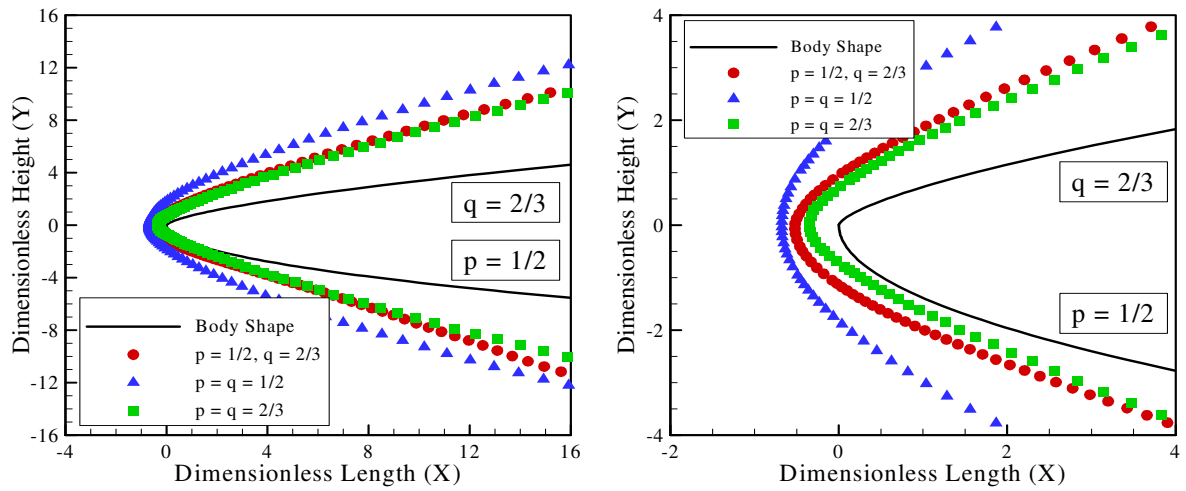

Figure 8: Shock-wave shapes on power-law leading edge defined by $p = 1/2$ and $q = 2/3$: (a) shock-wave on the total leading edge and (b) magnified view at the vicinity of the leading-edge nose.
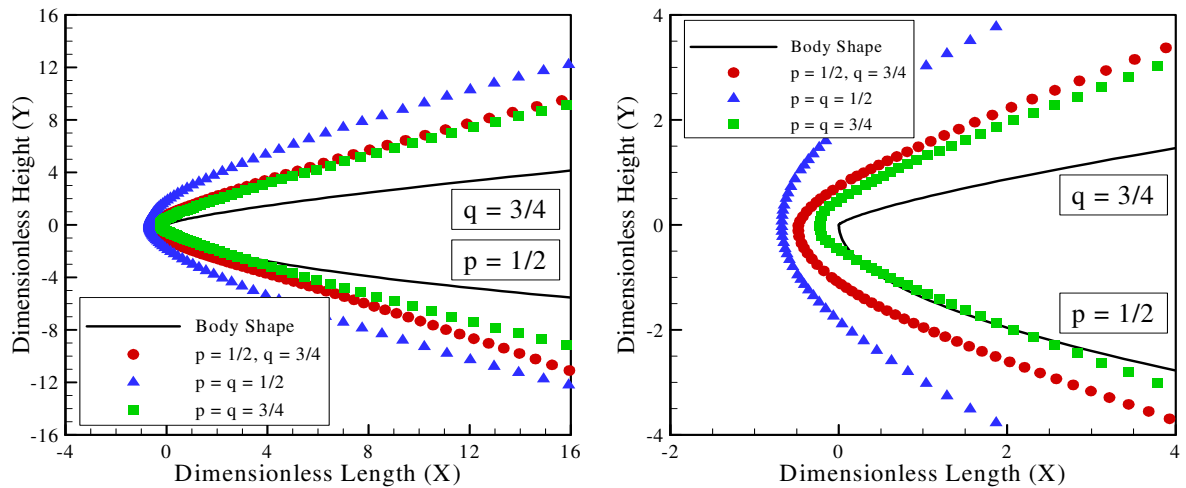

Figure 9: Shock-wave shapes on power-law leading edge defined by $p = 1/2$ and $q = 3/4$: (a) shock-wave on the total leading edge and (b) magnified view at the vicinity of the leading-edge nose.

8. CONCLUDING REMARKS

This study applies the Direct Simulation Monte Carlo method to investigate the shock-wave structure for a family of asymmetric or hybrid power-law shaped leading edges. The calculations have provided information concerning the nature of the shock-wave detachment distance, shock-wave thickness and shock-wave shape resulting from variations on the upper-surface power-law exponent for the idealized situation of two-dimensional hypersonic rarefied flow.

The analysis showed that the shock-wave structure was affected by changes on the leading-edge geometry. It was found that the shock-wave standoff and the shock-wave thickness decreased with increasing the upper-surface power-law exponent for the cases

investigated. As expected, it was also verified that the shock-wave center located more away of the body surface on the upper side than that on the lower side of the leading edges due to the leading-edge asymmetry.

REFERENCES

Alexander, F. J., Garcia, A. L., & Alder, B. J., 1998, Cell size dependence of transport coefficient in stochastic particle algorithms. *Physics of Fluids*, vol. 10, n. 6, pp. 1540-1542.

Alexander, F. J., Garcia, A. L., & Alder, B. J., 2000, Erratum: Cell size dependence of transport coefficient is stochastic particle algorithms. *Physics of Fluids*, vol. 12, n. 3, pp. 731-731.

Bird, G. A., 1981, Monte Carlo simulation in an engineering context. In Sam S. Fisher, ed., *Progress in Astronautics and Aeronautics: Rarefied gas Dynamics*, vol. 74, part I, pp. 239-255, AIAA, New York.

Bird, G. A., 1989, Perception of numerical method in rarefied gasdynamics. In E. P. Muntz, and D. P. Weaver and D. H. Capbell, eds., *Rarefied gas Dynamics: Theoretical and Computational Techniques*, vol. 118, pp. 374-395, Progress in Astronautics and Aeronautics, AIAA, New York.

Bird, G. A., 1994, *Molecular Gas Dynamics and the Direct Simulation of Gas Flows*. Oxford University Press, Oxford, England, UK.

Borgnakke, C. & Larsen, P. S., 1975, Statistical collision model for Monte Carlo simulation of polyatomic gas mixture. *Journal of computational Physics*, vol. 18, n. 4, pp. 405-420.

Cercignani, C., 1988, *The Boltzmann Equation and Its Applications*, Springer-Verlag, New York, NY.

Goonko, Y. P., Mazhul, I. I., & Markelov, G. N., 2000, Convergent-flow-derived waveriders. *Journal of Aircraft*, vol. 37, n. 4, pp. 647-654.

Guo, K. & Liaw, G.-S., 2001, A review: boundary conditions for the DSMC method. In *Proceedings of the 35th AIAA Thermophysics Conference*, AIAA Paper 2001-2953, Anaheim, CA.

Kim, B. S., Rasmussen, M. L., & Jischke, M. C., 1983, Optimization of waverider configurations generated from axisymmetric conical flows. *Journal of Spacecraft and Rockets*, vol. 20, n. 5, pp. 461-469.

Mangin, B., Benay, R., Chanetz, B., & Chpoun, A., 2006, Optimization of viscous waveriders derived from axisymmetric power-law blunt body flows. *Journal of Spacecraft and Rockets*, vol. 43, n. 5, pp. 990-998.

Mason, W. H. & Lee, J., 1994, Aerodynamically blunt and sharp bodies. *Journal of Spacecraft and Rockets*, vol. 31, n. 3, pp. 378-382.

Mazhul, I. I., & Rackchimov, R. D., 2004, Hypersonic power-law shaped waveriders in off-design regimes. *Journal of Aircraft*, vol. 41, n. 4, pp. 839-845.

Nonweiler, T. R. F., 1959, Aerodynamic problems of manned space vehicles. *Journal of the Royal Aeronautical Society*, vol. 63, Sept, pp. 521-528.

Rasmussen, M. L., 1980, Waverider configurations derived from inclined circular and elliptic cones. *Journal of Spacecraft and Rockets*, vol. 17, n. 6, pp. 537-545.

Rasmussen, M. L., & Ducan, B., 1995, Hypersonic waveriders generated from power-law shocks. AIAA Paper 95-6160.

Santos, W. F. N., & Lewis, M. J., 2002, Power-law shaped leading edges in rarefied hypersonic flow. *Journal of Spacecraft and Rockets*, vol. 39, n. 6, pp. 917-925.

Santos, W. F. N., & Lewis, M. J., 2005a, Calculation of shock wave structure over power-law bodies in hypersonic flow. *Journal of Spacecraft and Rockets*, vol. 42, n. 2, pp. 213-222.

Santos, W. F. N., & Lewis, M. J., 2005b, Aerothermodynamic performance analysis of hypersonic flow on power-law leading Edges. *Journal of Spacecraft and Rockets*, vol. 42, n. 4, pp. 588-597.

Santos, W. F. N., 2005, "Leading-edge bluntness effects on aerodynamic heating and drag of power law body in low-density hypersonic flow. *Journal of the Society of Mechanical Sciences and Engineering*, vol. 27, n. 3, pp. 236-241.

Santos, W. F. N., 2008a, "Physical and computational aspects of shock waves over power-law leading edges. *Physics of Fluids*, vol. 20, n. 1, pp. 1070631-11.

Santos, W. F. N., 2008b, "Direct simulation of hybrid power-law leading edge in hypersonic flow. *VIII Symposium on Computational Mechanics*, Belo Horizonte, MG, Brazil.